# Local electric properties of $\beta$-$Ag_{0.33}V_2O_5$ studied by $^{51}$V NMR

Akihiko HISADA*, Naoki FUJIWARA†, Touru YAMAUCHI[1], and Yutaka UEDA[1]

*Graduate School of Human and Environmental Studies, Kyoto University, Yoshida-nihonmatsu-cho, Sakyo-ku, Kyoto 606-8501, Japan*

[1]*Material Design and Characterization Laboratory, Institute for Solid State Physics, University of Tokyo, 5-1-5 Kashiwanoha, Kashiwa, Chiba 277-8581, Japan*

Local electric properties were studied on $\beta$-$Ag_{0.33}V_2O_5$, a pressure-induced superconductor, at ambient pressure using nuclear magnetic resonance (NMR) technique. Three crystalographically inequivalent Vi sites (i=1, 2, and 3) were identified from $^{51}$V-NMR spectra. We determined principal axes of the electric-field-gradient (EFG) tensor, electric quadrupole frequency, asymmetric parameter and Knight shift for each Vi site in a metallic phase and the following charge-ordering (CO) phase at low temperatures. The results suggested that electric properties for the V1 sites are similar to those for the V3 sites, whereas the V2 sites are independent of the V1 and V3 sites. The peculiarity in the metallic phase reflects the electric properties of the CO phase and it is attributable to the diagonal structure of the Vi orbitals.

KEYWORDS: vanadium bronze, quasi-one-dimensional conductor, charge ordering, NMR

## 1. Introduction

A family of $\beta$-vanadium bronze, $\beta$-$A_{0.33}V_2O_5$ (A=Li, Na, Ag), has offered an attractive stage in strongly correlated electron systems because it exhibits various phases on pressure-temperature ($P$-$T$) phase diagram; a metallic phase at high temperatures, a charge-ordering (CO) phase followed by an antiferromagnetic (AF) phase at low temperatures,[1–4] and pressure-induced superconductivity at pressures above 7 GPa.[5–8] The superconducting (SC) phase is adjacent to the CO phase observed at lower pressure region. The system is the first to exhibit superconductivity as a low dimensional vanadate. Superconductivity exhibits a bell-shaped $T_C$ curve with a $T_C$ optimum of about 7 K at 8 GPa on the $P$-$T$ phase diagram. In addition to these phase transitions, the cation (A=Li, Na, Ag) disorder-order transition occurs in the metallic phase.[1,9,10] The cation-, charge-, and spin-ordering temperatures, $T_A$, $T_{CO}$, and $T_{AF}$, respectively, are listed in Table I.

Since the discovery of the superconductivity, no further information has been obtained other than $P$ dependence of $T_C$ because of experimental difficulties under high pressures. There still remain two major problems; one is the pairing symmetry and the other is behavior

*E-mail: A.Hisada@s01.mbox.media.kyoto-u.ac.jp
†E-mail: naokif@mbox.kudpc.kyoto-u.ac.jp

near the phase boundary. The detailed boundary has not still been fixed; one possibility is phase separation between the CO and SC phases, and the other is crossover between them. In relation to this problem, a novel superconducting mechanism such as a charge-fluctuation mediated mechanism has been proposed.[13)]

Besides the superconductivity, the insulating phase including the CO and AF phases, induced by metal-insulator transition (MIT) at low pressures below 7 GPa, also exhibits unique features. The successive charge and magnetic orderings are realized although the electron density is very low; a $3d^1$ electron exists among six V sites as formally expressed as $\beta$-$A_{0.33}(V^{4+}+5V^{5+})_{0.33}O_5$, where $V^{4+}$ is a magnetic ion with spin S=1/2 and $V^{5+}$ is a nonmagnetic ion. Several charge-distribution models were proposed after the discovery of the superconductivity because of a complicated crystal structure; there exist three crystalographically inequivalent Vi sites, V1, V2, and V3. Each of them forms quasi-one-dimensional coupling along $b$ axis.

$\beta$-$Na_{0.33}V_2O_5$, a prototype of the series, has been investigated so far using several experimental techniques. Yamaura *et. al.* observed from the X-ray diffraction the lattice modulation along the $b$ direction with twofold ($2b$) and sixfold ($6b$) periodicity below $T_A$ and $T_{CO}$, respectively, and proposed a rectangle-type charge-ordering model below $T_{CO}$, where $V^{4+}$ ions are located on every three V2 sites in the $b$ axis.[10,14)] Nagai *et. al.* also observed from the neutron diffraction the same lattice modulation along the $b$ direction.[15)] Moreover, they suggested charge disproportionation with threefold ($3b$) periodicity from the magnetic Bragg reflections, and attributed the $6b$ lattice modulation below $T_{CO}$ to the $2b$ lattice modulation multiplied by the $3b$ charge modulation. They proposed a charge-distribution model which includes a nonmagnetic V site in every three Vi sites along the $b$ axis. Relative charge density for the Vi sites was estimated as 3:2:3, respectively. Meanwhile another model was proposed from electron spin resonance (ESR); $3d^1$ electrons are primarily located on the V1 zigzag chains and the charges occupy six consecutive V1 sites below $T_{CO}$.[16)] $^{51}$V- and $^{23}$Na-NMR measurements were investigated based on the charge-distribution model proposed by the neutron diffraction measurement and relative charge density for the Vi sites was estimated as 3:1:1.[17,18)] The NMR results suggest that $3d^1$ electrons are mainly located on the V1 sites. They also reported the changes of nuclear spin-lattice relaxation rate $1/T_1$ at every transition temperatures.[19)]

$\beta$-$Ag_{0.33}V_2O_5$, an isomorphic compound of $\beta$-$Na_{0.33}V_2O_5$, has an advantage over $\beta$-$Na_{0.33}V_2O_5$ because $\beta$-$Ag_{0.33}V_2O_5$ is crystallographically stable whereas $\beta$-$Na_{0.33}V_2O_5$ is very sensitive to Na concentration; $\beta$-$Na_{0.32}V_2O_5$ hardly exhibits metallic behavior in the whole $T$ range, although $\beta$-$Na_{0.33}V_2O_5$ is metallic at room temperature.[8)] In $\beta$-$Ag_{0.33}V_2O_5$ we proposed a much simple model in the previous NMR and zero field resonance (ZFR) works; a $3d^1$ electron is located on a rung of V1-V3 and V2-V2 ladders like a proton molecular orbital. The

electric quadrupole frequency and internal field which correspond to a half of a $3d^1$ electron per a magnetic Vi site were observed in the CO and AF phases, respectively. These results give an evidence of the charge sharing.[20)]

$\beta$-$Sr_{0.33}V_2O_5$, which possesses more charge than $\beta$-$Na_{0.33}V_2O_5$ or $\beta$-$Ag_{0.33}V_2O_5$, exhibits a similar charge ordering, although the ground state properties are different.[6,10,21–23)] The $^{51}$V-NMR measurements were performed in the metallic phase and remarkable charge disproportion was reported in the V2-V2 ladders. Development of ferromagnetic correlation at low temperatures was suggested from Knight shift and $1/(T_1T)$.[24)]

At present a variety of phenomena were observed so far for $\beta$-vanadium bronzes. For the systematical understanding of the series NMR measurement is one of the most powerful methods because the method is site selective, namely it can specify microscopic information of $3d^1$ electrons on each Vi site independently. In the previous work, we proposed a charge ordering model in $\beta$-$Ag_{0.33}V_2O_5$. In this paper, we will extend the previous work to the metallic phase focusing on the electric-field-gradient (EFG) tensor.

## 2. Crystal structure

The series of compounds consist of three kinds of crystalographically inequivalent Vi sites. As shown in Fig. 1, a complicated crystal structure was often used in the early studies; the edge-shared zigzag chains of $V1O_6$ octahedra, the corner-shared two-leg ladders of $V2O_6$ octahedra, and the edge-shared zigzag chains of $V3O_5$ pyramids.[10,21,25)]

However, a much simpler theoretical model has been presented recently by Doublet and Lepetit.[26)] Fig. 2 shows weakly interacting two-leg ladder model based on extended Hückel tight-binding calculations; the $V1O_5$ and $V3O_5$ pyramids form corner-shared two-leg ladders, and the two $V2O_5$ pyramids also form another ones independently. Cations are located in the tunnels of the framework and occupy one of two nearest-neighboring sites as shown in both Figs. 1 and 2.

The crystalographical symmetry of the uniform metallic phase above $T_A$ is $C2/m$. Below $T_A$, this symmetry changes to $P2_1/a$ and the $b$ cell parameter becomes twice as large as that above $T_A$, because of the zigzag ordering of the cations. Although it retains the same space group below $T_{CO}$, the $b$ cell parameter becomes six times as large as that above $T_A$.[10,14,21)] Thus, the sixfold superstructure is deeply concerned with the charge ordering.

## 3. Experimental

$^{51}$V-NMR measurements were performed using a needlelike single crystal prepared by a self-flux method with a CZ furnace. The crystal grew up in the direction of the $b$ axis, the chain or leg direction. The volume of the crystal was $0.5\times4\times0.5$ mm$^3$. We used a conventional pulsed-NMR spectrometer. NMR spectra were measured at a frequency of 59.00 MHz for the field ($\boldsymbol{H}$ ) parallel ($\parallel$) or perpendicular ($\perp$) to the $b$ axis. We attached a hand-made rotation

apparatus to a NMR probe for the case of $\boldsymbol{H} \perp b$. Hereafter we express the direction of the $\boldsymbol{H}$ as an angle $\theta$ from the [1 0 -1] direction as shown in Fig. 2. The error margin was within $\pm$ 5 degrees caused in an initial setting. A powder pellet sample of 8-mm diameter and 6-mm length was used in ZFR measurement. ZFR spectra were measured up to 170 MHz with a separation of 0.25 MHz / point at 4.2 K.

## 4. Results

### *4.1* $^{51}$*V NMR for* $\boldsymbol{H} \| b$

We measured $^{51}$V-NMR spectra for $\boldsymbol{H} \| b$ in the $T$ range of 4.2-300 K. The pattern of $^{51}$V(I=7/2)-NMR spectra changed at 200, 90, and 27 K corresponding to the transition temperatures $T_A$, $T_{CO}$, and $T_{AF}$, respectively. Typical $\boldsymbol{H}$-swept spectra in the metallic, CO, and AF phases are presented in Fig. 3. The spectra in the metallic phase were measured at above and below $T_A$. There appear seven peaks with a constant separation for a V site owning to the nuclear quadrupole interaction. We observed three sets of signals originating from three crystallographically inequivalent V sites above $T_{AF}$. The sites were assigned from the $\theta$ dependence of the EFG for $\boldsymbol{H} \perp b$ as described in subsection 5.1. Information of the peak separations for $\boldsymbol{H} \| b$ appearing in Fig. 3 is reflected in the fitting curves for $\boldsymbol{H} \perp b$ in Figs. 6(b)- 8(b) via an asymmetric parameter $\eta$ of the EFG.

As shown in Figs. 3(c) and 8(a), there appeared broad basal signals in addition to the sharp peaks in the CO phase. As shown in Fig. 4, relative intensity of the sharp peaks becomes small compared to the broad signals with increasing $\tau$, which is a separation of two rf pulses. This implies that the spin-spin relaxation time $T_2$ of the sharp peaks is shorter than that of the broad signals. In general, nonmagnetic site possesses much larger $T_2$ than that of the magnetic site. Therefore the sharp peaks and broad basal signals are attributable to magnetic $V^{4+}$ like sites and nonmagnetic $V^{5+}$ sites, respectively.

We also measured $\tau$ dependence of the spin-echo intensity for the first satellite for the V1 sites. The position of the satellite is shown in Fig. 4 as bold-type arrows on a dashed line. The $\tau$ dependence is shown in Figs. 5 (a) and (b). Fig. 5(b) is an expansion of Fig. 5(a). We also plotted the $\tau$ dependence in the metallic phase for comparison. The decay curve in the CO phase consists of two components with shorter and longer characteristic time constants. Moreover, the decay curve with a shorter time constant is similar to that in the metallic phase. Therefore the shorter component is shown to originate from the magnetic sites.

In the AF phase, the sharp signals arising from magnetic sites are wiped out and only broad signals are observed. It is because the signals of magnetic sites are shifted into higher frequencies owning to the large internal field caused by the AF magnetic ordering.

### *4.2 $^{51}V$ NMR for $\boldsymbol{H}\perp b$ and site assignment*

We measured $^{51}$V-NMR spectra for the $\boldsymbol{H}$ direction of $\theta$=47 and 200° at temperatures above $T_{AF}$. Typical spectra at 230, 130, and 80 K are shown in Figs. 6(a), 7(a), and 8(a), respectively. These directions correspond to the principal axes of the EFG tensor for three Vi sites which are determined in subsection 5.1. The direction of $\theta$=47° corresponds to the first and second principal axes for the V1 and V2 sites, respectively, whereas that of $\theta$=200° corresponds to the first principal axis for the V3 sites.

We also measured $\theta$ dependence of the $^{51}$V-NMR peaks at 230, 130, and 80 K, as shown in Figs. 6(b), 7(b), and 8(b), respectively. The dotted and solid lines indicate fitting curves for the central peaks and the third satellite peaks, respectively (See Eq. (1) and (2)). Some peaks that seem to split into two such as the peaks at $\theta$=200° in the metallic phase are influenced by a large free induction decay (FID) overlapped with the spin echo. In such a case we estimated the resonance field taking mean values of the two positions.

The V1, V2, and V3 sites were assigned using the directions of the first principal axes of the EFG tensor. According to the theoretical investigation, hybridization of V orbitals forms weakly interacting two-leg ladders as shown in Fig. 2. V orbitals in the ground state are expected to be $d_{xy}$, therefore the first principal axis should turn to the apical direction of each $VO_5$ pyramid. In other words, the splitting due to the EFG should become the maximum when the $\boldsymbol{H}$ is applied to the apical direction. Our experimental results are consistent with the theoretical model, namely the directions of the first principal axes agree with the apical directions, the deviations between them are only 23, 7, and 24 degrees for the V1, V2, and V3 sites, respectively.

The principal axes of the Knight shift, a direction where the central peak becomes the maximum, were estimated to be 175, 100, and 5° for the V1, V2, and V3 sites, respectively. In the case of $d_{xy}$ symmetry, the principal axes of the Knight shift should be the same with those of the EFG. However, the directions of the principal axes do not agree with each other. In other words, the principal axes of the Knight shift do not coincide with the apical directions of the pyramids. The discrepancy would arise from distortion of the local $VO_5$ pyramids. Thus the Knight shift offers less information than the EFG for the site assignment.

## 5. Analysis

### *5.1 Fitting parameters for three Vi sites*

Seven peaks with an equal frequency separation originate from the interaction of nuclear quadrupole moment Q with the EFG. When parameter $\theta_Q$ represents a polar angle between the $\boldsymbol{H}$ and the first principal axis, and parameter $\phi_Q$ represents an azimuthal angle between the $\boldsymbol{H}$ and the third principal axis, the frequency separation for an arbitrary $\boldsymbol{H}$ direction is

expressed as

$$\nu^{(1)}_{m\to m-1} = \frac{\nu_Q}{2}(m-\frac{1}{2})(3\cos^2\theta_Q - 1 - \eta\sin^2\theta_Q\cos 2\phi_Q)$$

$$(m = i + 1/2, |i| \leq 3) \quad (1)$$

where $\nu_Q = 3e^2qQ/2I(2I-1)h$ is the electric quadrupole frequency and $q = \partial^2V/\partial z^2 (= V_{ZZ})$ is the EFG for the first principal axis. Asymmetric parameter $\eta$ is defined as $\eta = |V_{XX} - V_{YY}|/|V_{ZZ}|$ using diagonal elements of the EFG tensor. In the case that the $\boldsymbol{H}$ directs the first principal axis, the frequency span between the two first satellites is given as $2\nu_Q$.

The Knight shift $K$ is defined as $K \equiv (H_{ref} - H_0)/H_0$ where $H_0$ represents the field of the central peaks for the V1, V2, and V3 sites. The reference field $H_{ref}$ is calculated as 52.71 kOe from the NMR frequency of 59.00 MHz and the gyromagnetic ratio $\gamma_N$=1.1193 MHz/kOe of $^{51}$V. The angle dependence of the Knight shift is caused by the asymmetry of hyperfine field:

$$K(\theta) = K_l + K_a(3\cos^2\theta_K - 1) \quad (2)$$

where $K_l$ and $K_a$ are symmetric and asymmetric terms, respectively, and $\theta_K$ represents an angle between the $\boldsymbol{H}$ and the symmetry axis. The parameters $\nu_Q$, $\eta$, $K_l$, and $K_a$ at 230, 130, and 80 K are estimated from the $^{51}$V-NMR results with $\boldsymbol{H}\perp b$ (Figs. 6(b)- 8(b)). The $\theta$ dependence of the peak positions is analyzed based on Eqs. (1) and (2). We used the definition of the EFG tensor, $|V_{XX}| \leq |V_{YY}| \leq |V_{ZZ}|$ and $V_{XX} + V_{YY} + V_{ZZ} = 0$ in the analysis. The value of $\nu_Q$, $\eta$, $K_l$, $K_a$ are listed in Table II. Hereafter we express these values for each Vi sites as $\nu_Q$(Vi), $\eta$(Vi), $K_l$(Vi), $K_a$(Vi), respectively.

As shown in Table II, there is a similarity between the V1 and V3 sites. In the metallic phase, the value of $\eta$ and $|K_a|$ for the V1 sites are close to those for the V3 sites, whereas those for the V2 sites are relatively large. As for $\nu_Q$ and $K_l$, the trend is clearly seen below $T_A$. These features mean that local electric properties for the V1 sites are similar to those for the V3 sites, whereas the V2 sites are independent of the V1 and V3 sites. In the CO phase, the same features are also seen for $\nu_Q$, $K_l$, and $K_a$, however, $\eta$(V1) becomes the largest among three Vi sites. This fact is closely related with peculiarity of the EFG tensor for the V1 sites.

### *5.2 T dependence of the EFG tensor*

In this subsection, we present $T$ dependence of the peak separations for the three principal axes and $\eta$ for each Vi site. The maximum peak separation in Figs. 9(a)- 11(a) corresponds to $\nu_Q$ shown in Table II. Closed squares in Figs. 9(a)- 11(a) represent the peak separations measured for two of the three principal axes, $\nu^{(1)}_{m\to m-1}(\theta_Q = 0^\circ)(= \nu_Q)$, $\nu^{(1)}_{m\to m-1}(\theta_Q = 90^\circ, \phi_Q = 0^\circ)$, and $\nu^{(1)}_{m\to m-1}(\theta_Q = 90^\circ, \phi_Q = 90^\circ)$. As mentioned above, the first principal axis for the V1 sites and the second principal axis for the V2 sites correspond to the direction of $\theta$=47°, and the first principal axis for the V3 sites corresponds to the direction

of $\theta$=200°. Another principal axis for each Vi site corresponds to the $b$ axis. Closed circles in Figs. 9(a)- 11(a) represent calculated values for the other principal axis using the equation $V_{XX}+V_{YY}+V_{ZZ}=0$. Figs. 9(b), 10(b), and 11(b) show the $T$ dependence of $\eta$(V1), $\eta$(V2) and $\eta$(V3), respectively. The EFG tensor for each Vi site exhibits different features with each other.

(i) $\nu_Q$(V1) gradually increases just below $T_A$ and $T_{CO}$ with decreasing temperature. The EFG tensor for the V1 sites shows unique behavior; the $b$ axis, the third principal axis in the metallic phase, turns into the second principal axis in the CO phase (Fig. 9(a)). Simultaneously, $\eta$(V1) is enhanced below $T_{CO}$ (Fig. 9(b)), reflecting the lattice distortion caused in the CO phase.

(ii) $\nu_Q$(V2) is smaller than $\nu_Q$(V1) and $\nu_Q$(V3) in each phase. It shows slight change throughout the $T$ range between 30 K and 300 K (Fig. 10(a)). On the other hand, $\eta$(V2) is larger than $\eta$(V1) and $\eta$(V3) in the metallic phase. This shows that the EFG tensor for the V2 sites is the most anisotropic among the three Vi sites.

(iii) $\nu_Q$(V3) shows similar behavior to $\nu_Q$(V1). It is almost constant in the metallic phase and becomes a little bit larger below $T_{CO}$.(Fig. 11(a)) The EFG tensor for the V3 sites is the most isotropic, namely, $\eta$(V3) is the smallest among the three Vi sites (Fig. 11(b)).

As a result, although $\eta$(V1) in the CO phase becomes the largest among three Vi sites, the similarity of the electric properties between the V1 and V3 sites is shown from the $T$ dependence of $\nu_Q$ throughout the temperatures above $T_{AF}$.

### *5.3 Local spin alignment*

The similarity between the V1 and V3 sites is also seen in the previous ZFR study in the AF phase.[20] The peaks for the magnetic V1 sites were observed at 21.50 and 71.25 MHz and those for the V3 sites were observed at almost the same positions, 24.75 and 73.00 MHz. On the other hand, the V2 sites were observed at different positions, i.e. 48.00 and 98.75 MHz. In this paper, we investigate the ZFR results considering that the V2 sites are independent of the V1 and V3 sites, though we assumed the charge distribution as uniform for all Vi sites in the previous work.

ZFR frequency $f_{peak}$ is proportional to the internal field $H_n$ at each Vi site; $f_{peak}=\gamma_N|H_n|$. The internal field $H_n$, composed of Fermi-contact field $H_F$ and dipole field $H_{dip}$, is expressed as

$$|\boldsymbol{H}_n| = 2k < S > \sqrt{A^{\parallel 2}\cos^2\theta_n + A^{\perp 2}\sin^2\theta_n} \tag{3}$$

where $A^{\parallel(\perp)}$ is a sum of the hyperfine coupling of $H_F$ and the dipole coupling for spin parallel (perpendicular) to the EFG maximum direction, i.e. the first principal axis, and $k$ is a reduction factor due to the covalent effect with oxygen, and $\theta_n$ is the angle between spin moment and the EFG maximum direction. We used $k$=0.8 as a typical value, and the values of $A^{\parallel}$ and

$A^{\perp}$ are calculated to be -230 and 35 kOe, respectively. When an electron is shared by $n$ sites, $< S >$ should be expressed as

$$< S >= \frac{1}{2n}. \tag{4}$$

X-ray diffraction shows the sixfold periodicity in the leg direction below $T_{CO}$, implying that possible choice of $n$ is $n = 1$ to 6.

Fig. 12(a) shows the $\theta_n$ dependence of the resonance frequency calculated from Eqs. (3) and (4) for $n = 1$ to 6. As for the V1 and V3 sites, the signals below 24.75 MHz are explained for $n = 2$ to 6, while the signals above 71.25 MHz are explained only for $n = 1$ or 2. Therefore the value of $n$ is uniquely determined as 2. On the other hand, the signals for the V2 sites at 48.00 and 98.75 MHz are explained by both of $n = 1$ and 2. However, note that $\nu_Q$(V2) in the CO phase is intermediate between representative values of magnetic $V^{4+}O_5$ pyramids observed in $CaV_2O_5$ (0.96 MHz) and nonmagnetic $V^{5+}O_5$ pyramids in $V_2O_5$ (0.07 MHz), the charge density for each magnetic V2 site is estimated to be 1/2 to 1/4. Therefore the value of $n$ for the V2 sites is also uniquely determined as 2. As a result, we conclude that a $3d^1$ electron is essentially shared within two V sites both for the V1-V3 rungs and the V2-V2 rungs, and the validity of the previous model as shown in Fig. 12(b) was confirmed. In this model, the spin moments with the opposite directions also satisfy Eq. (3) and they could form the antiferromagnetic alignment in the AF phase. The existence of two kinds of spin moments for each Vi site is attributable to the crystallographical peculiarity in the CO phase: X-ray diffraction revealed the sixfold lattice modulation along the $b$ axis making locally inequivalent pyramid structure on the Vi site. Therefore two V1-V3 rungs located on crystalographically inequivalent position would make two kinds of spin directions. On the other hand, two sets of V2-V2 magnetic rungs would be induced by local arrangement of the V1-V3 magnetic rungs, although two V2-V2 rungs are located on equivalent positions.

## 6. Discussions

### *6.1 Peculiar metallic phase*

We have found from the EFG analyses that the electric properties for the V1 sites are similar to those for the V3 sites in the metallic and CO phases, whereas the V2 sites are independent of the V1 and V3 sites. This feature is consistent with that obtained in the AF phase where the charge sharing of $3d^1$ electron within the V1-V3 or V2-V2 rungs is suggested. Two quasi-one-dimensional conduction paths, namely V1-V3 and V2-V2 ladders, are likely formed in the metallic phase, and charge ordering would be realized in each path in the CO phase. Such a peculiarity is expected from the tight-binding model in which the orbitals of the V1 or V3 sites are diagonal to those of the V2 sites.[26] The microscopic model gives an explanation for the semiconducting resistivity along the a and c axes in the metallic phase.[1]

*6.2 Charge ordering model*

Now we focus on the CO phase. To maintain electrical neutrality, magnetic rung and nonmagnetic rung should be in the ratio of 1 to 2. The magnetic rungs are expected to align with threefold lattice periodicity to avoid Coulomb repulsion. This threefold charge periodicity has also been reported for $\beta$-$Na_{0.33}V_2O_5$. However, the charge-distribution pattern is different from the present case; $\beta$-$Na_{0.33}V_2O_5$ consists of two magnetic rungs and a nonmagnetic rung. The reason why the charge-distribution pattern differs depending on materials is not certain at present. The charge distribution may be sensitive to the relationship between hopping and Coulomb repulsions between neighboring sites, and as a result depends on detailed environments of the materials.

The idea of charge sharing within a rung like hydrogen molecule is rather promising to understand why the ground state of $\beta$-$Ag_{0.33}V_2O_5$ is an AF ordering state, whereas that of $\beta$-$Sr_{0.33}V_2O_5$ is a singlet state. The former includes a magnetic rung with S=1/2 aligned in every three rungs along the leg direction (Fig. 13(a)), then coupling of two rungs seems difficult because such rungs would be located on isolated positions to avoid Coulomb interaction. On the other hand, the latter includes one nonmagnetic rungs in every three rungs along the leg direction. As a result, two rungs with S=1/2 are located on the nearest neighboring positions (Fig. 13(b)). Therefore singlet formation accompanied with lattice distortion would decrease the total energy. In real material, situation may be much complicated; however, essential property can be explained by the charge sharing within a lang.

## 7. Summary

We measured $^{51}$V NMR on $\beta$-$Ag_{0.33}V_2O_5$ for the metallic and CO phases. Three crystalographically inequivalent Vi sites (i=1, 2, and 3) were assigned from the $^{51}$V-NMR spectra and we determined the principal axes of the EFG tensor, the electric quadrupole frequency $\nu_Q$, the asymmetric parameter $\eta$, and the Knight shift $K$ for each Vi site in each phase. These parameters and the $T$ dependence of the EFG tensor suggest that electric properties for the V1 sites are similar to those for the V3 sites, whereas the V2 sites are independent of the V1 and V3 sites. This result shows that the peculiar metallic phase reflecting the electric properties of the CO phase is realized. The peculiarity is attributable to the diagonal structure of the Vi orbitals.

## Acknowledgment

We would like to thank H. Seo, M. Itoh, S. Fujimoto, S. Yamamoto, H. Ikeda, Y. Uwatoko, M. Hedo, N. Takeshita and T. Nakanishi for valuable discussions. We also thank J. Yamaura for X-ray analysis of the crystal axes. This work was supported by a Grant-in-Aid (20·1187) for Scientific Research from the Japan Society for the Promotion of Science and a Grant-in-Aid (KAKENHI 17340107) from the Ministry of Education, Science and Culture, Japan.

## References


1) H. Yamada and Y. Ueda, J. Phys. Soc. Jpn. **68** (1999) 2735.
2) Y. Ueda, J. Phys. Soc. Jpn. Suppl. B **69** (2000) 149.
3) M. Itoh, N. Akimoto, H. Yamada, M. Isobe, and Y. Ueda, J. Phys. Soc. Jpn. Suppl. B **69** (2000) 155.
4) Y. Ueda, H. Yamada, M. Isobe, and T. Yamauchi, J. Alloys Compd. **317-318** (2001) 109.
5) T. Yamauchi, Y. Ueda, and N. Môri, Phys. Rev. Lett. **89** (2002) 057002.
6) Y. Ueda, M. Isobe, and T. Yamauchi, J. Phys. Chem. Solids **63** (2002) 951.
7) T. Yamauchi, M. Isobe, and Y. Ueda, Solid State Sci. **7** (2005) 874.
8) T. Yamauchi and Y. Ueda, Phys. Rev. B **77** (2008) 104529.
9) Y. Nakai, S. Kagoshima, and H. Nagasawa, J. Phys. Soc. Jpn. **51** (1982) 697.
10) J. Yamaura, M. Isobe, H. Yamada, T. Yamauchi, and Y. Ueda, J. Phys. Chem. Solids **63** (2002) 957.
11) A. Hisada, N. Fujiwara, T. Yamauchi, Y. Ueda, M. Hedo, and Y. Uwatoko, J. Magn. Magn. Mater. **310** (2007) 893.
12) T. Yamauchi, H. Ueda, and Y. Ueda, Physica C **460-462** (2007) 66.
13) J. Merino and R. H. McKenzie, Phys. Rev. Lett. **87** (2001) 237002.
14) J. Yamaura, T. Yamauchi, E. Ninomiya, H. Sawa, M. Isobe, H. Yamada, and Y. Ueda, J. Magn. Magn. Mater. **272-276** (2004) 438.
15) S. Nagai, M. Nishi, K. Kakurai, Y. Oohara, H. Yoshizawa, H. Kimura, Y. Noda, B. Grenier, T. Yamauchi, J. Yamaura, M. Isobe, Y. Ueda, and K. Hirota, J. Phys. Soc. Jpn. **74** (2005) 1297.
16) M. Heinrich, H.-A. Krug von Nidda, R. M. Eremina, A. Loidl, Ch. Helbig, G. Obermeier, and S. Horn, Phys. Rev. Lett. **93** (2004) 116402.
17) T. Suzuki, I. Yamauchi, M. Itoh, T. Yamauchi, and Y. Ueda, Phys. Rev. B **73** (2006) 224421.
18) M. Itoh, I. Yamauchi, T. Kozuka, and T. Suzuki, Phys. Rev. B **74** (2006) 054434.
19) I. Yamauchi, M. Itoh, T. Yamauchi, and Y. Ueda, Phys. Rev. B **74** (2006) 104410.
20) A. Hisada, N. Fujiwara, T. Yamauchi, Y. Ueda, M. Hedo, and Y. Uwatoko, Phys. Rev. B **78** (2008) 012402.
21) C. Sellier, F. Boucher, and E. Janod, Solid State Sci. **5** (2003) 591.
22) V. Ta Phuoc, C. Sellier, and E. Janod, Phys. Rev. B **72** (2005) 035120.
23) T. Yamauchi, H. Ueda, J. Yamaura, and Y. Ueda, Phys. Rev. B **75** (2007) 014437.
24) T. Waki, M. Takigawa, T. Yamauchi, J. Yamaura, H. Ueda, and Y. Ueda, J. Phys. Chem. Solids **68** (2007) 2143.
25) E. Deramond, J.-M. Savariault, and J. Galy, Acta Crystallogr. **C50** (1994) 164.
26) M. L. Doublet and M. B. Lepetit, Phys. Rev. B **71** (2005) 075119.
27) H. Iwase, M. Isobe, Y. Ueda, and H. Yasuoka, J. Phys. Soc. Jpn. **65** (1996) 2397.

Fig. 1. (Color online) Crystal structure of $\beta$-$A_{0.33}V_2O_5$ (A=Li,Na,Ag) series. $V1O_6$ octahedra and $V3O_5$ pyramids form edge-shared zigzag chains and $V2O_6$ octahedra form corner-shared two-leg ladders along the $b$ axis. Cations occupy one of two nearest-neighboring sites in an $ac$ plane.[10,21,25)]

Fig. 2. (Color online) Two-leg ladder model proposed by Doublet and Lepetit. The covalent bonds of V orbitals form two-leg ladders. V1 and V3 sites form two-leg ladders and two V2s sites form the other independent ones. The inset represents $VO_5$ pyramid.[26)]

Fig. 3. (Color online) $^{51}$V-NMR spectra for $\boldsymbol{H} \| b$ in the metallic, charge-ordering (CO), and antiferromagnetic (AF) phases. Disorder-order transition of $Ag^+$ occurs at 200 K.

Fig. 4. Pulse separation ($\tau$) dependence of $^{51}$V-NMR spectra for $\boldsymbol{H} \| b$ in the CO phase. Relative intensity of basal broad signals increases with increasing $\tau$. Echo-decay curves in Figs. 5(a) and 5(b) were measured at the position shown by bold-type arrows.

Fig. 5. $\tau$ dependence of the spin-echo intensities in the CO and the metallic phases. Open circles and closed squares represent the decay curves in the CO phase and the metallic phase, respectively. (a) Decay curve in the CO phase consists of two components. The shorter one is similar to that in the metallic phase. (b) An expansion of Fig. 5 (a). Modulation of the Spin-Echo Intensity is due to the nuclear quadrupole interaction.

Fig. 6. (Color online) (a) $^{51}$V-NMR spectra in the metallic phase ($T$=230 K). (b) angle ($\theta$) dependence of the $^{51}$V-NMR peaks. The dotted and solid lines indicate fitting curves for the central peaks and the third satellite peaks, respectively. Each $Z_{Vi}$ represents the angle of the first principal axis of the EFG tensor for each Vi sites.

Fig. 7. (Color online) (a) $^{51}$V-NMR spectra in the metallic phase with Ag ordering ($T$=130 K). (b) $\theta$ dependence of the $^{51}$V-NMR peaks. The dotted and solid lines indicate fitting curves for the central peaks and the third satellite peaks, respectively. Each $Z_{Vi}$ represents the angle of the first principal axis of the EFG tensor for each Vi site.

Fig. 8. (Color online) (a) $^{51}$V-NMR spectra in the CO phase ($T$=80 K). (b) $\theta$ dependence of the $^{51}$V-NMR peaks. The dotted and solid lines indicate fitting curves for the central peaks and the third satellite peaks, respectively. Each $Z_{Vi}$ represents the angle of the first principal axis of the EFG tensor for each Vi site.[20)]

Fig. 9. (Color online) (a) $T$ dependence of the peak separation for the V1 sites. The maximum peak separation corresponds to the electric quadrupole frequency $\nu_Q$ shown in Eq. (1). (b) $T$ dependence of the asymmetric parameter $\eta$ for the V1 sites.

Fig. 10. (Color online) (a) $T$ dependence of the peak separation for the V2 sites. The maximum peak separation corresponds to the electric quadrupole frequency $\nu_Q$ shown in Eq. (1). (b) $T$ dependence of the asymmetric parameter $\eta$ for the V2 sites.

Fig. 11. (Color online) (a) $T$ dependence of the peak separation for the V3 sites. The maximum peak separation corresponds to the electric quadrupole frequency $\nu_Q$ shown in Eq. (1). (b) $T$ dependence of the asymmetric parameter $\eta$ for the V3 sites.

Fig. 12. (Color online) (a) $\theta_n$ dependence of the resonance frequency calculated for $n = 1$ to 6, $\theta_n$ being the angle between spin moment and the EFG maximum direction. Solid and dotted straight lines indicate resonance frequencies of ZFR peaks. (b) The directions of spin moments obtained for each Vi site.

Fig. 13. Scheme of charge-sharing within a rung. (a) Rungs with $S = 1/2$ are isolated in every three lattices along the leg direction due to Coulomb interaction for $\beta$-$A^{+}_{0.33}V_2O_5$, giving a reason why the ground state of $\beta$-$Ag_{0.33}V_2O_5$ is magnetic. (b) Two $3d^1$ electrons exist on the nearest neighboring rungs along the leg direction for $\beta$-$A^{2+}_{0.33}V_2O_5$, which could cause singlet pairing. The scenario explains phenomenologically why the ground state of $\beta$-$Sr_{0.33}V_2O_5$ is a singlet.

Table I. Cation-, charge-, and spin-ordering temperatures, $T_A$, $T_{CO}$, and $T_{AF}$ at ambient pressure. In $\beta$-$Sr_{0.33}V_2O_5$ , the cation disorder-order transition already occurs at room temperature, and the ground state of insulating phase is not an antiferromagnetic states, but a spin-gapped state.[7,8,10–12)]

| compound | $V^{4+}/V^{5+}$ | $T_A$ (K) | $T_{CO}$ (K) | $T_{AF}$ (K) |
|---|---|---|---|---|
| $\beta$-$Li_{0.33}V_2O_5$ | 1/5 | - | 180 | 7 |
| $\beta$-$Na_{0.33}V_2O_5$ | 1/5 | 260 | 136 | 24 |
| $\beta$-$Ag_{0.33}V_2O_5$ | 1/5 | 200 | 90 | 27 |
| $\beta$-$Sr_{0.33}V_2O_5$ | 2/4 | >RT | 170 | - |

Table II. The electric quadrupole frequency $\nu_Q$, the asymmetric parameter of the EFG $\eta$, and the symmetric and asymmetric terms of the Knight shift $K_l$ and $K_a$ in the metallic phase ($T$=230 K ), the metallic phase with Ag ordering ($T$=130 K ), and the CO phase ($T$=80 K ).

| $T$ (K) | Site | $\nu_Q$(MHz) | $\eta$ | $K_l$(%) | $K_a$(%) |
|---|---|---|---|---|---|
| 230 | V1 | 0.35 | 0.10 | -0.22 | -0.13 |
| | V2 | 0.28 | 0.46 | -0.32 | -0.37 |
| | V3 | 0.31 | 0.06 | -0.13 | -0.13 |
| 130 | V1 | 0.39 | 0.17 | -0.26 | -0.09 |
| | V2 | 0.28 | 0.63 | -0.54 | -0.48 |
| | V3 | 0.36 | 0.07 | -0.17 | -0.17 |
| 80 | V1 | 0.44 | 0.57 | -0.07 | -0.09 |
| | V2 | 0.27 | 0.36 | -0.66 | -0.30 |
| | V3 | 0.42 | 0.13 | -0.02 | -0.11 |

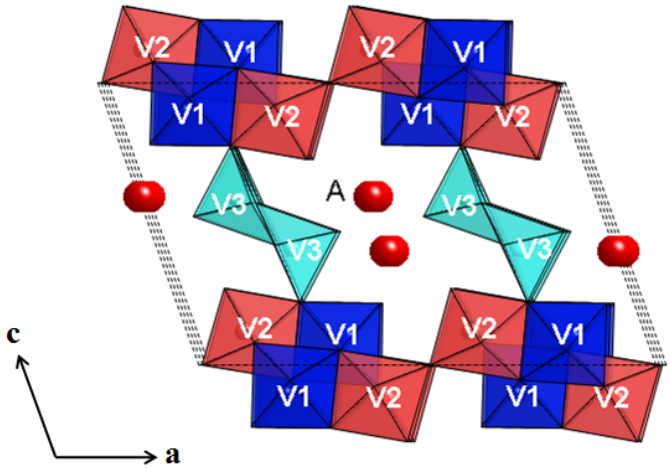


Fig. 1.

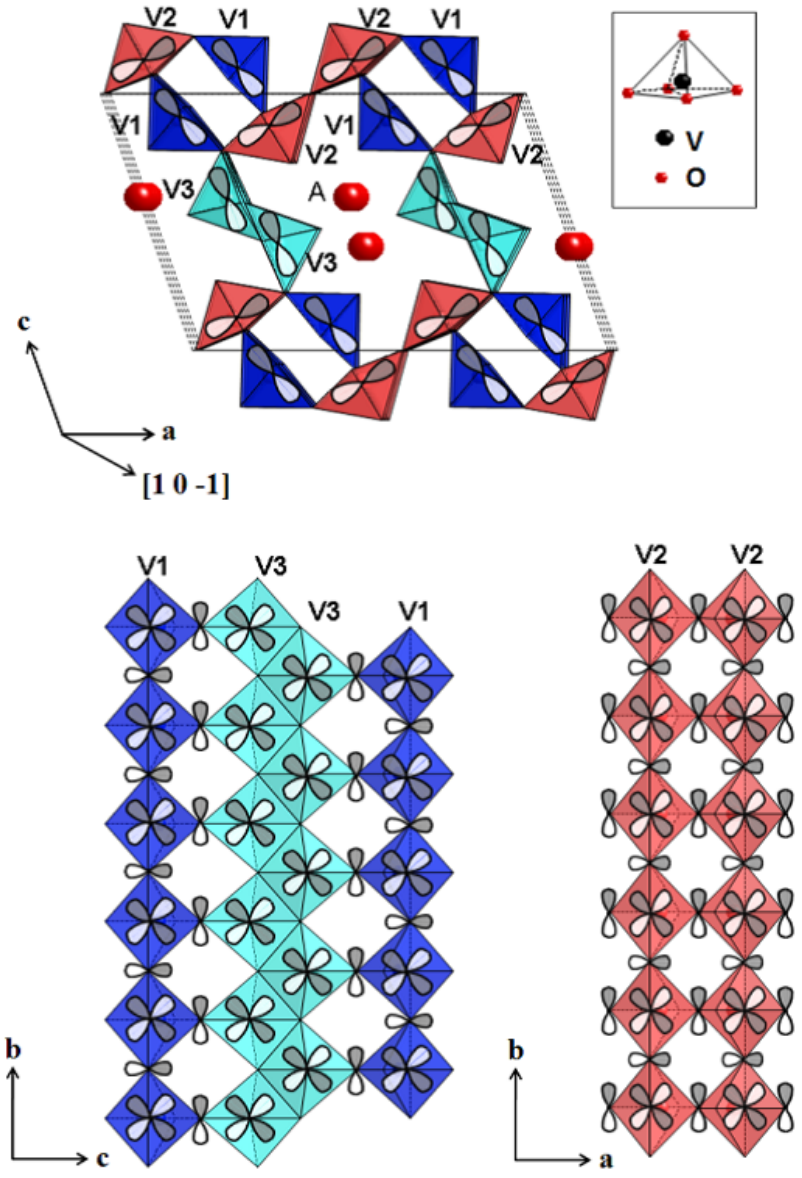


Fig. 2.

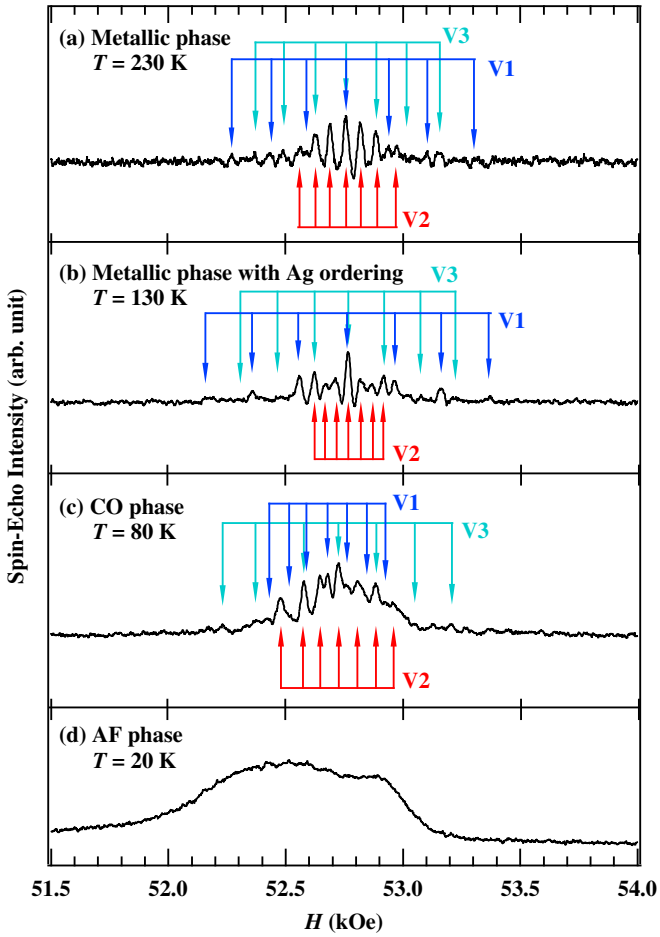
(a) Metallic phase
T = 230 K
V3
V1
V2
(b) Metallic phase with Ag ordering
T = 130 K
V3
V1
V2
(c) CO phase
T = 80 K
V1
V3
V2
(d) AF phase
T = 20 K
Spin-Echo Intensity (arb. unit)
51.5
52.0
52.5
53.0
53.5
54.0
H (kOe)

Fig. 3.

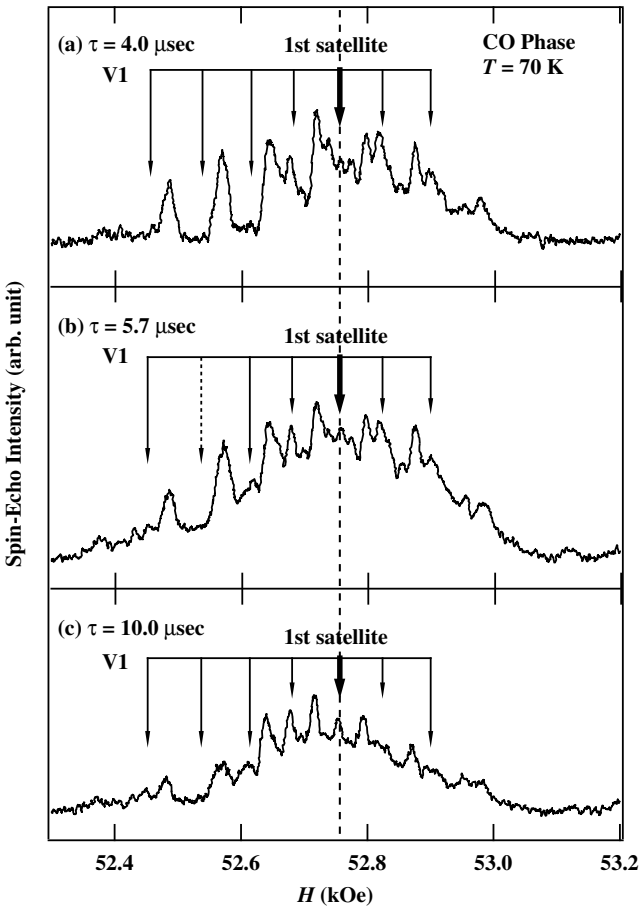
(a) τ = 4.0 μsec
1st satellite
V1
CO Phase
T = 70 K
(b) τ = 5.7 μsec
1st satellite
V1
(c) τ = 10.0 μsec
1st satellite
V1
Spin-Echo Intensity (arb. unit)
52.4
52.6
52.8
53.0
53.2
H (kOe)

Fig. 4.

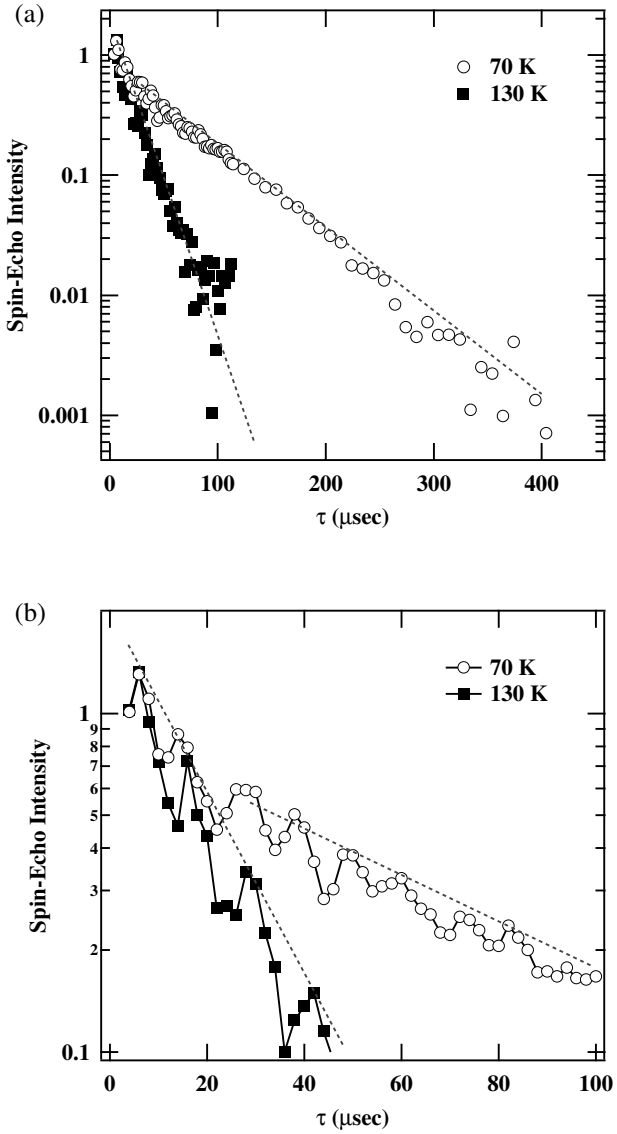
(a)
70 K
130 K
Spin-Echo Intensity
1
0.1
0.01
0.001
0
100
200
300
400
τ (μsec)
(b)
70 K
130 K
Spin-Echo Intensity
1
9
8
7
6
5
4
3
2
0.1
0
20
40
60
80
100
τ (μsec)

Fig. 5.

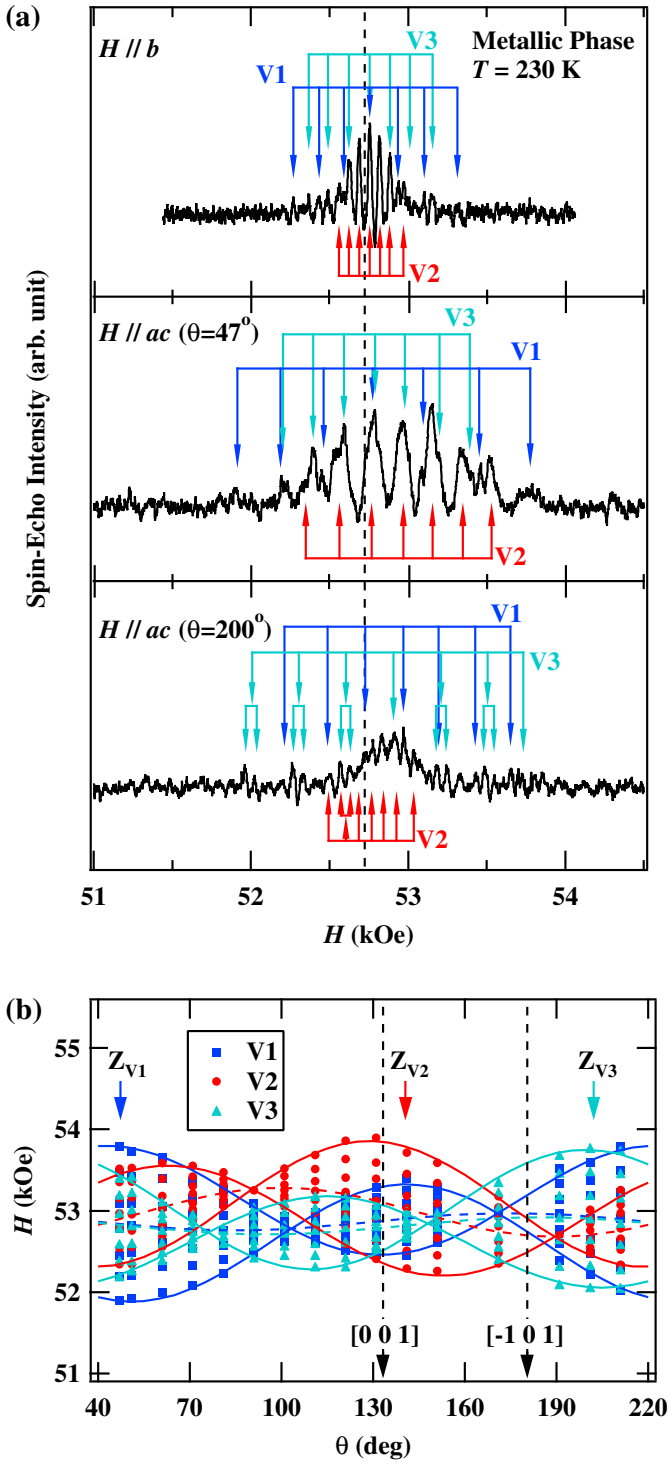
(a)
H // b
V3
V1
Metallic Phase
T = 230 K
V2
H // ac (θ=47°)
V3
V1
V2
H // ac (θ=200°)
V1
V3
V2
Spin-Echo Intensity (arb. unit)
51
52
53
54
H (kOe)
(b)
55
54
53
52
51
H (kOe)
Z_V1
Z_V2
Z_V3
V1
V2
V3
[0 0 1]
[-1 0 1]
40
70
100
130
160
190
220
θ (deg)

Fig. 6.

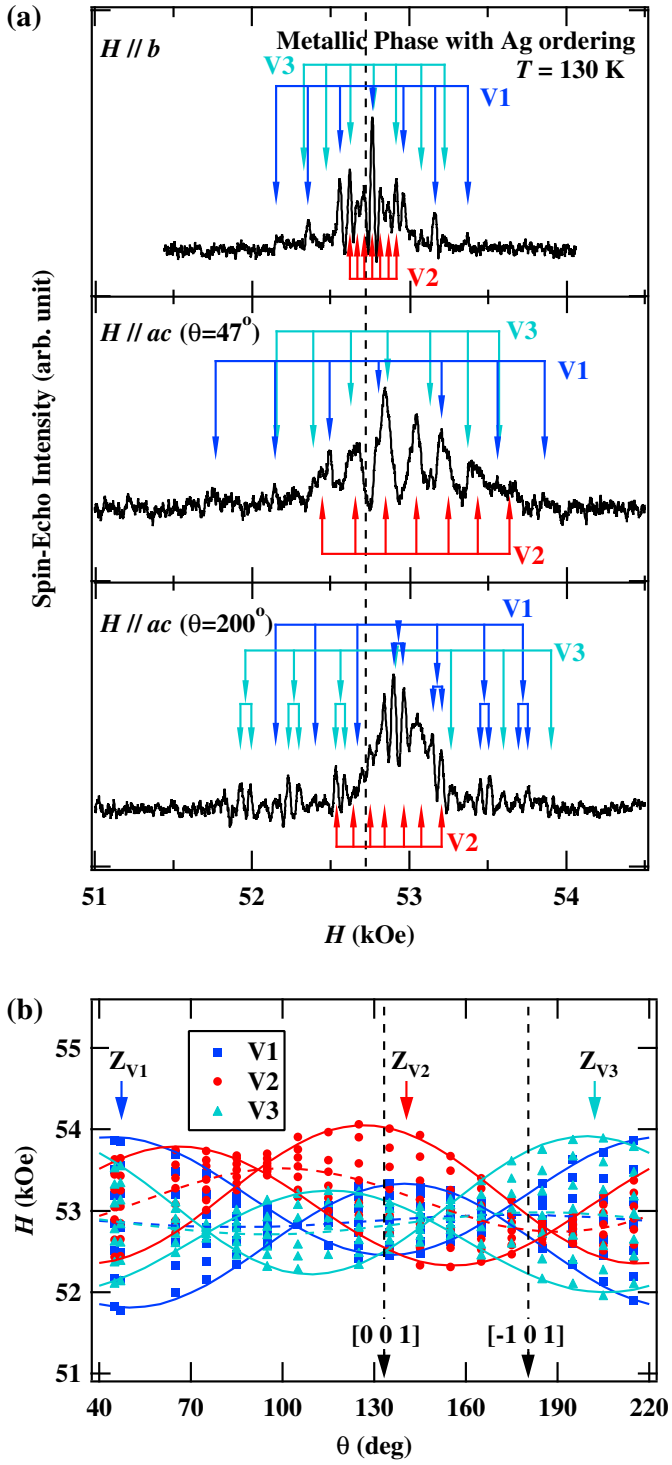
(a)
H // b
Metallic Phase with Ag ordering
T = 130 K
V3
V1
V2
H // ac (θ=47°)
V3
V1
V2
H // ac (θ=200°)
V1
V3
V2
Spin-Echo Intensity (arb. unit)
51
52
53
54
H (kOe)
(b)
Z_V1
Z_V2
Z_V3
V1
V2
V3
55
54
53
52
51
H (kOe)
[0 0 1]
[-1 0 1]
40
70
100
130
160
190
220
θ (deg)

Fig. 7.

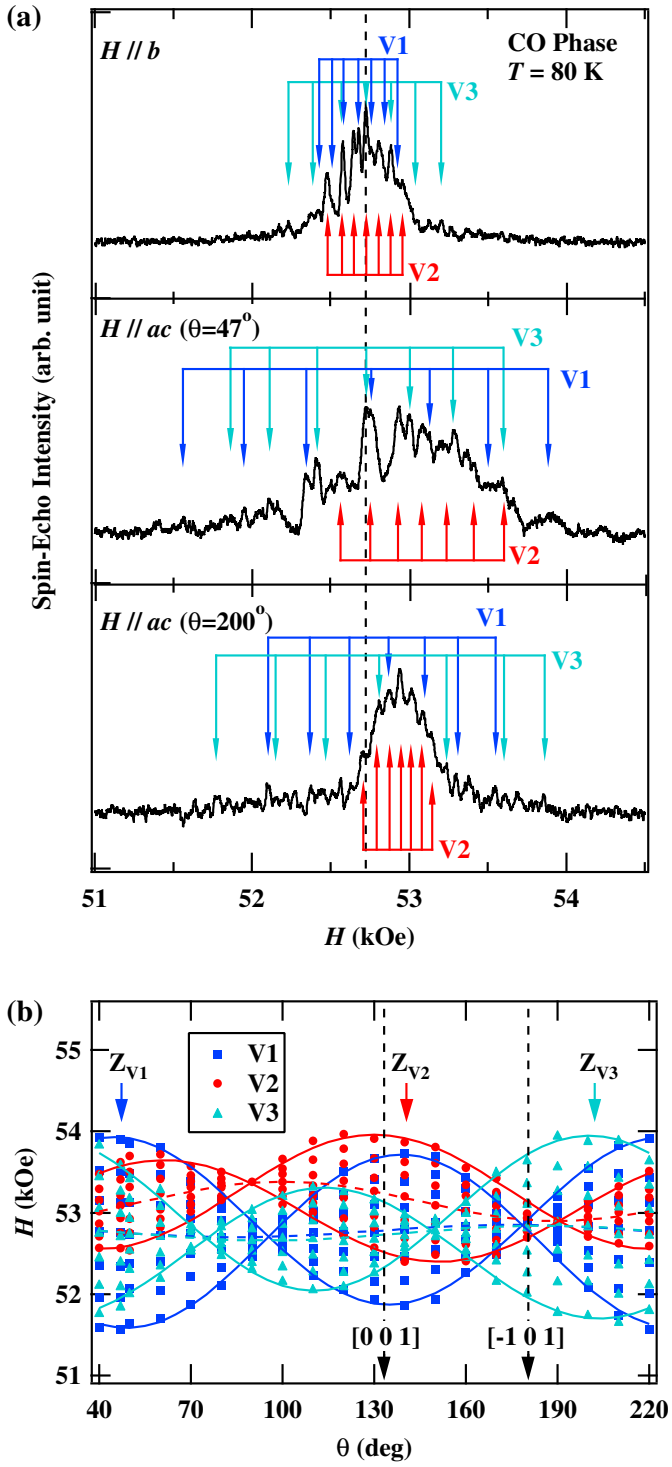
(a)
H // b
V1
V3
CO Phase
T = 80 K
V2
H // ac (θ=47°)
V3
V1
V2
H // ac (θ=200°)
V1
V3
V2
Spin-Echo Intensity (arb. unit)
51
52
53
54
H (kOe)
(b)
55
54
53
52
51
H (kOe)
Z_V1
Z_V2
Z_V3
V1
V2
V3
[0 0 1]
[-1 0 1]
40
70
100
130
160
190
220
θ (deg)

Fig. 8.

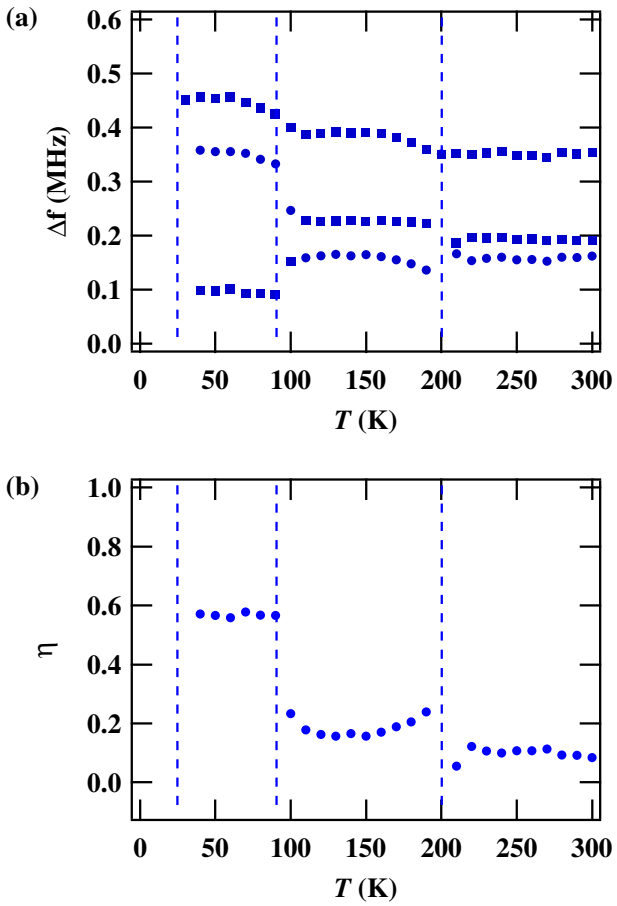
(a)
Δf (MHz)
0.0
0.1
0.2
0.3
0.4
0.5
0.6
0
50
100
150
200
250
300
T (K)
(b)
η
0.0
0.2
0.4
0.6
0.8
1.0
0
50
100
150
200
250
300
T (K)

Fig. 9.

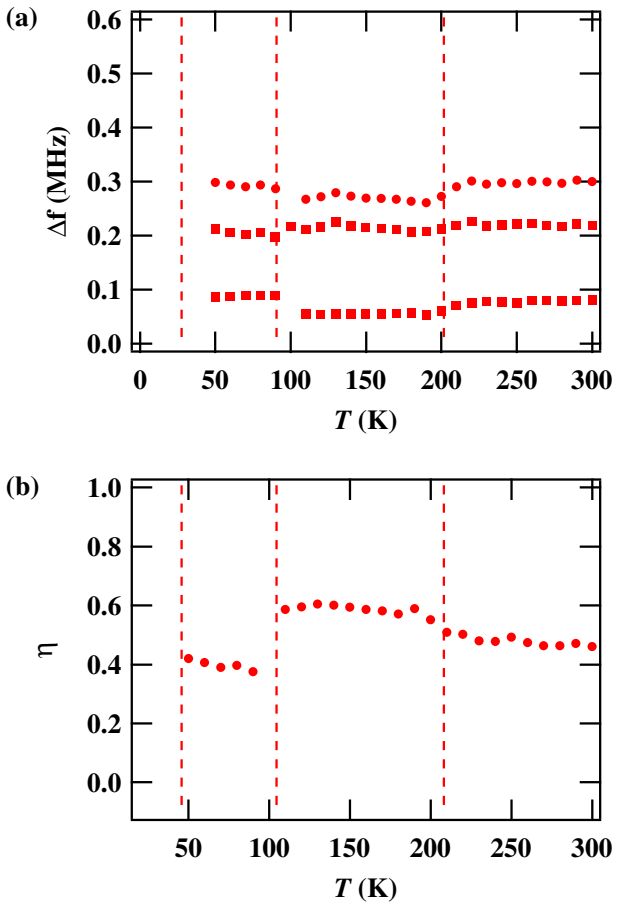
(a)
0.6
0.5
0.4
0.3
0.2
0.1
0.0
Δf (MHz)
0
50
100
150
200
250
300
T (K)
(b)
1.0
0.8
0.6
0.4
0.2
0.0
η
50
100
150
200
250
300
T (K)

Fig. 10.

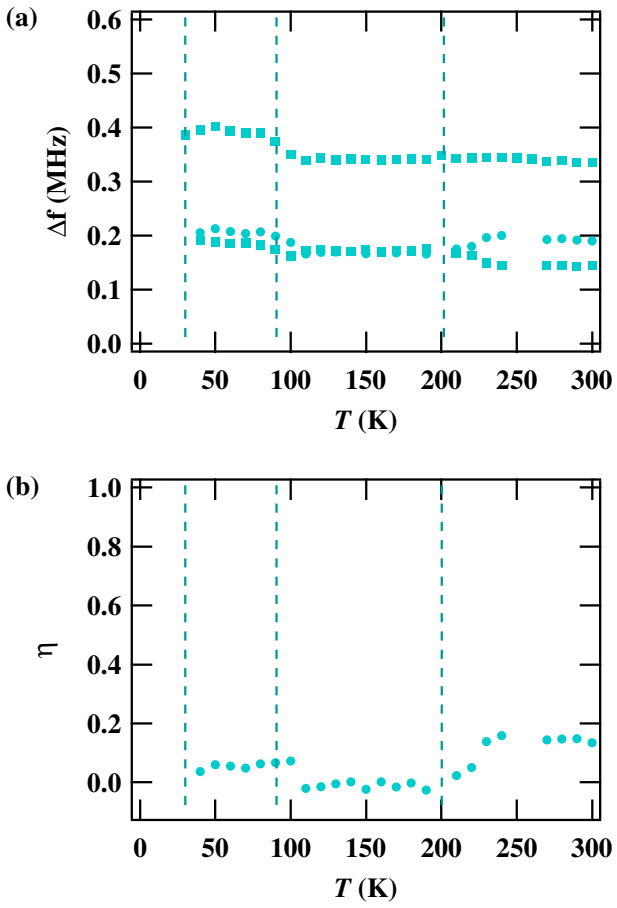
(a)
Δf (MHz)
0.6
0.5
0.4
0.3
0.2
0.1
0.0
0
50
100
150
200
250
300
T (K)
(b)
η
1.0
0.8
0.6
0.4
0.2
0.0
0
50
100
150
200
250
300
T (K)

Fig. 11.

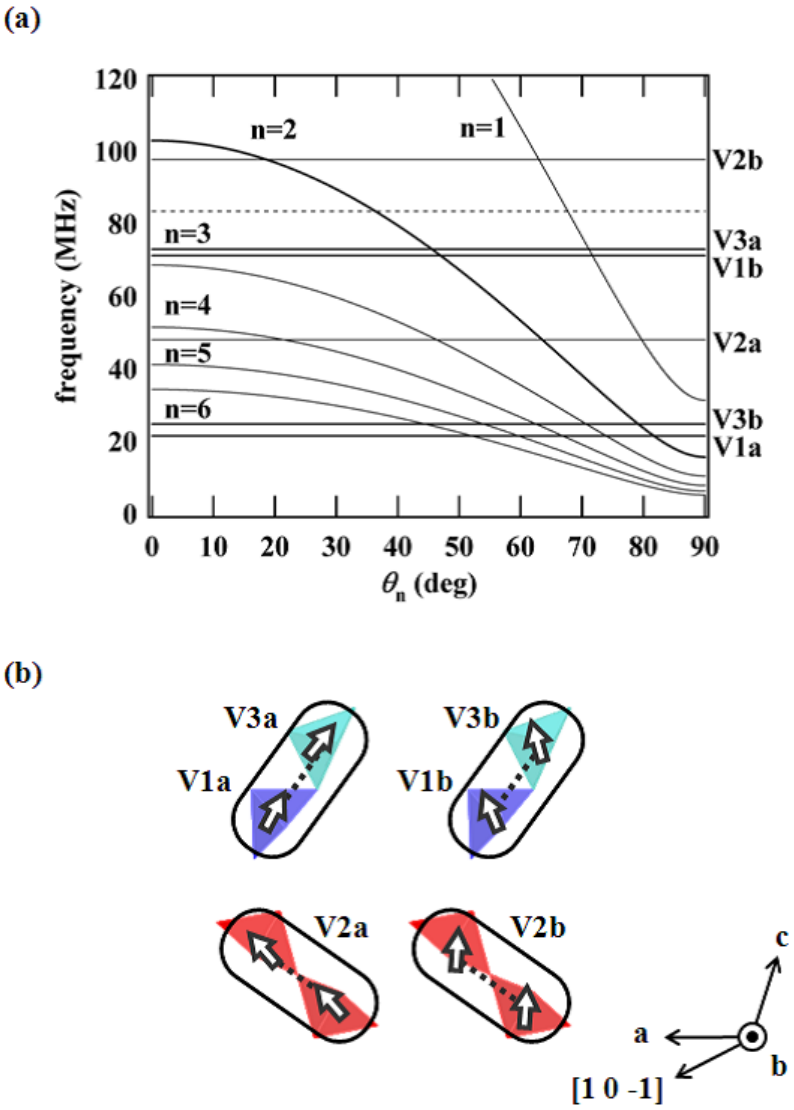
(a)
120
100
80
60
40
20
0
frequency (MHz)
n=2
n=1
n=3
n=4
n=5
n=6
V2b
V3a
V1b
V2a
V3b
V1a
0 10 20 30 40 50 60 70 80 90
θn (deg)
(b)
V3a
V1a
V3b
V1b
V2a
V2b
c
a
b
[1 0 -1]

Fig. 12.

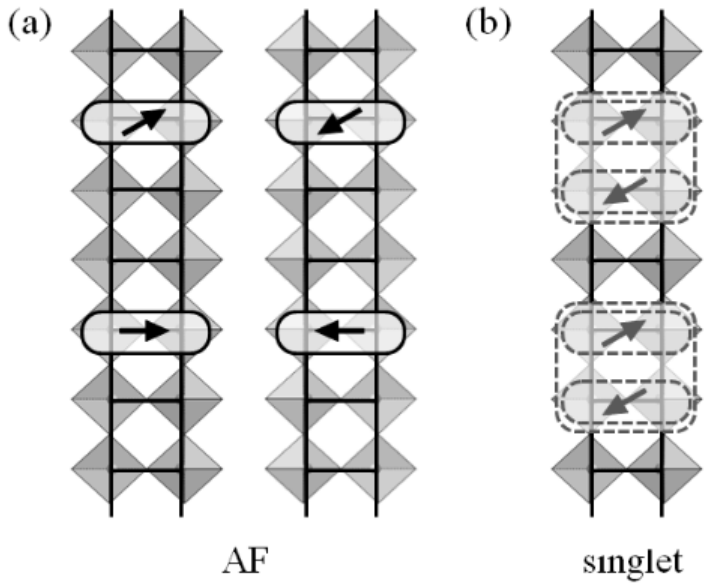


Fig. 13.